

Gate-Controlled Electron Quantum Interference Logic Devices

Josef Weinbub^{*1}, Mauro Ballicchia², and Mihail Nedjalkov²

¹Christian Doppler Laboratory for High Performance TCAD, Institute for Microelectronics, TU Wien, Austria

²Institute for Microelectronics, TU Wien, Austria

Recent advances in electron quantum optics [1–10] show the breathtaking progress in utilizing the electron’s wave nature. Inspired by these advances, we propose a new type of electron quantum interference logic device (eQILD), where an electron wave is coherently injected into a two-dimensional (2D) wave guide and controlled via two gates. Interference effects lead to different current levels in output channels and are utilized for classical logic gates. The operating principle is shown by means of dynamic quantum Wigner and classical simulations considering coherent/ballistic transport. Contrary to other advanced information processing approaches no magnetism nor bosonic systems are required [11]. The eQILD is inherently compatible with conventional integrated circuits and thus provides an attractive alternative towards advanced low-power information processing devices with the performance only limited by the single-electron source frequency being in the GHz regime [2].

Quantum interference devices have a long history, ranging from superconducting applications [12–14] to early investigations into logic [15]. In contrast, the eQILD uses a different operational principle (Figure 1). For the 2D wave guide we consider a $22 \times 40 \text{ nm}^2$ molybdenum disulfide (MoS_2) single-layer; a 2D semiconductor of the family of transition metal dichalcogenides (TMDs). The initial choice of MoS_2 is based on excellent transport, fabrication, and insulator compatibility properties and its wide-spread research focus [16, 17]. However, the choice of wave guide material is not limited to MoS_2 , other types of 2D semiconductors [16] or 2D electron gases (2DEGs; e.g. (Al)GaAs heterostructures) are in principle compatible with the eQILD design. The wave guide is conceptually insulated by a cap and a substrate layer on the top and bottom, respectively, and offers reflective boundary conditions along $x = 0 \text{ nm}$ and $x = 22 \text{ nm}$ (Figure 2 and 3). The gates are embedded in the cap layer: Based on the charge and shape of the gates and the distance between them, the transport domain, the output channel walls (potential energy of 0.1 eV and dimensions $2 \times 10 \text{ nm}^2$ centered at $x = 7 \text{ nm}$ and 15 nm , respectively, and ranging from $y = 30 - 40 \text{ nm}$), and the boundaries, we calculate the corresponding potential energy distribution in the

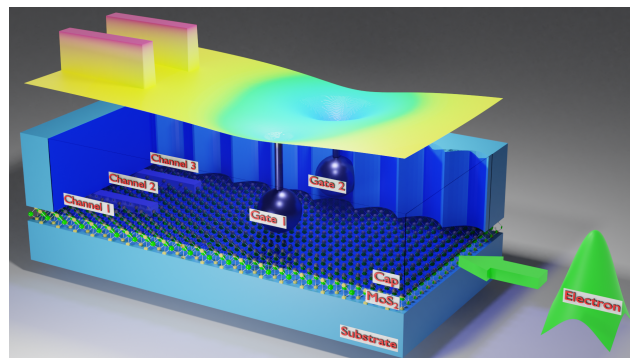


Figure 1: Schematic representation of the eQILD. An exemplary potential energy distribution of the wave guide derived from biased gates and the device structure is shown on top. The blue cap layer is partially made transparent to show the inside of the device.

channel as is discussed below (see an exemplary potential energy distribution overlaid in Figure 1). Further considering the physical characteristics of the injected electrons, we use the calculated potential energy distribution to simulate the electron transport (quantum and classical) in the 2D wave guide by stochastic evolution simulations [18] (see Supplementary Information A) for various gate configurations and calculate the current levels in the output channels.

The simulation setup conceptually resembles a double-slit experiment, where single electrons are shot consecutively towards a screen, until a stationary (steady-state) interference pattern is obtained [19, 20]. The probabilistic interpretation is of equivalent independent (uncorrelated) experiments aiming at accumulating sufficient statistics. Electrons with energies of 71 meV enter on one side of the device and have a dwelling time in the femtosecond regime, underlining the sole limitation of performance on the electron source frequency [2].

Single-layer MoS_2 is a direct-bandgap (1.8 eV) semiconductor, which makes it well-suited for low-power applications [21]. First principles band structure calculations showed that for n-type single-layer MoS_2 the K, K’ valleys, which are well-separated in energy from the satellite valleys, are most relevant for low-field transport. A parabolic band with electron mass $m = 0.48m_0$ (see (1) in Supplementary Information A), with m_0 being the mass of the free electron, gives a perfect description of the conduction band valley around the K point.

^{*}josef.weinbub@tuwien.ac.at

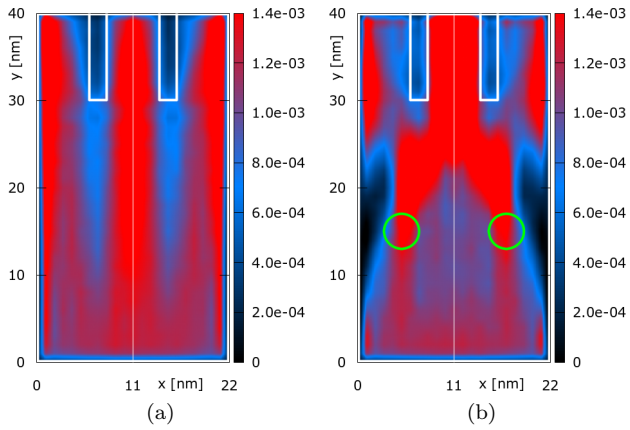


Figure 2: Distribution of quantum electron density [a.u.] for two symmetric gate configurations: $\phi_{G_1} = \phi_{G_2} = 0$ V (a) and $\phi_{G_1} = \phi_{G_2} = 0.21$ V (b). The output channel walls are shown in white. Green circles indicate location of gates.

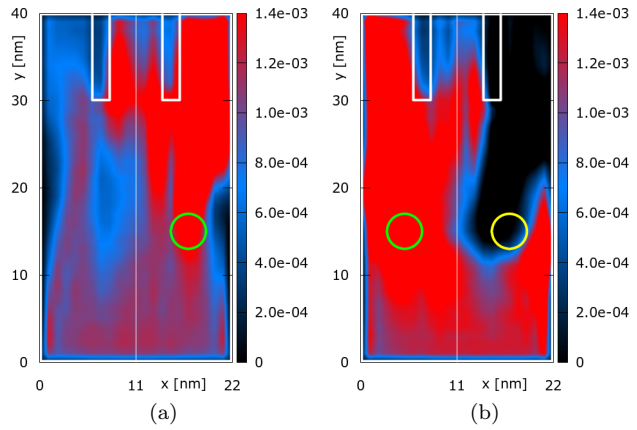


Figure 3: Distribution of quantum electron density [a.u.] for two asymmetric gate configurations: $\phi_{G_1} = 0$ V and $\phi_{G_2} = 0.21$ V (a) and $\phi_{G_1} = 0.21$ V and $\phi_{G_2} = -0.21$ V (b). The yellow circle indicates the location of the negatively charged gate.

The metal gates are each modeled as solid spheres with a radius of 2 nm positioned 3 nm (relative to the sphere center) above the wave guide, resulting in 1 nm cap oxide material (calcium fluoride – CaF_2 [16]) between the surface of the gates and the MoS_2 . In the following discussions of the calculated 2D quantum electron densities in the wave guide we consider various gate bias configurations in terms of the electric potential ϕ (potential energy $V = -q\phi$ with q the electron charge): A negative or positive gate bias represents a repulsive barrier or an attractive well for the electrons, respectively.

Figure 2a considers no applied bias to the gates, Gate 1 (G_1) and Gate 2 (G_2). Electrons are injected in y -direction at the bottom (see green wave-packet in Fig. 1). The two wall potentials impose strong non-local effects upon the electrons, shown in particular by the reduced density in y -direction below the walls. The electron density is thus equally split into the three output channels, following the symmetry of the walls. Figure 2b shows the electron density for a symmetric gate bias configuration, i.e., $\phi_{G_1} = \phi_{G_2} = 0.21$ V. The resulting peak of the superimposed electric potential of the two gates, as determined by the gate and device geometry, is 0.17 V on the MoS_2 surface, i.e., both gates act as *attractive* wells. As a result, a focusing effect materializes: The majority of the electron density is guided towards output channel 2 (the central channel).

Figure 3a shows the electron density for an asymmetric gate bias configuration, i.e., $\phi_{G_1} = 0$ V and $\phi_{G_2} = 0.21$ V, corresponding to a resulting peak superimposed electric potential on the MoS_2 surface of 0.14 V, i.e., ϕ_{G_2} acts as an *attractive* well in front of output channel 3 (right channel): The majority of the electron density is thus guided towards channel 3, less so towards channel 2, and considerably less to channel 1 (left channel). Figure 3b shows the electron density for another representative asymmetric gate configuration where the gates are biased in an opposing manner,

i.e., $\phi_{G_1} = 0.21$ V and $\phi_{G_2} = -0.21$ V. This configuration corresponds to a resulting peak superimposed electric potential on the MoS_2 surface of 0.11 V in front of channel 1, and a repulsive barrier of -0.11 V in front of channel 3. In this case the electron density guided towards channel 3 is almost completely blocked and the majority of the electron moves towards channel 1; a considerably smaller part of the electron density enters channel 2. The effects of penetration and tunneling into the output channel walls seen in both cases of Figure 3 is a clear indication of the quantum character of the electron evolution.

Figure 4 shows the calculated quantum currents for a representative selection of ϕ_{G_1} biases relative to fixed ϕ_{G_2} biases in the three output channels. The current at the output of each channel has been calculated by integrating the current density along the corresponding output cross-section. In turn, the current density is calculated from the first-order moment of the electron distribution function. Figure 4a considers the case of $\phi_{G_2} = 0$ V; G_2 is thus not active (see a similar scenario in Figure 3a albeit for G_1). For negative ϕ_{G_1} biases, ϕ_{G_1} repulses the majority of the current to channel 3, with a similar inverted behavior for positive biases with respect to channel 1. In case of $\phi_{G_1} = 0$ V, the electron is equally distributed between all three output channels as expected from device symmetry considerations, which corresponds to the scenario depicted in Figure 2a. The negative and positive ϕ_{G_1} bias ranges *seem to offer a mirrored* behavior, however, both ranges offer entirely different physical scenarios of repulsion and attraction, leading to different interactions between the electrons and the potential energy landscape and thus to different current levels. Therefore, a fully-mirrored behavior is not to be expected. Figure 4b considers the case of $\phi_{G_2} = 0.105$ V. The negative bias range offers similar general behavior as for $\phi_{G_2} = 0$ V (see Figure 4a), however, for the symmetric case $\phi_{G_1} = \phi_{G_2} = 0.105$ V a focusing effect with respect to channel 2 manifests (similar to Figure 2b).

159 A further increased ϕ_{G_1} bias results in a deeper well po- 220
 160 tential at G_1 over G_2 , thus the majority of the current 221
 161 manifests in channel 1. Figure 4c considers the case of 222
 162 $\phi_{G_2} = 0.21$ V; G_2 acts as an even stronger attractive 223
 163 well. Yet another intriguing example of non-locality is 224
 164 seen here for negative biases: Although ϕ_{G_2} has doubled 225
 165 (compare with Figure 4b), the current in channel 226
 166 1 & 2 stays roughly the same but in channel 3 (located 227
 167 behind G_2) is reduced further, demonstrating the wave 228
 168 nature of the evolution. 229

169 Table 1 provides an extended overview of the gate
 170 bias to channel current relations and together with Table
 171 2 shows various exemplary interpretations as logic
 172 gates: Particularly important are *universal* NAND and
 173 NOR gates as both are *functionally complete* and as
 174 such can be used to implement all possible Boolean
 175 functions [22]. In classical logic, a NAND gate is de-
 176 fined by the *truth table* $00 \rightarrow 1, 01 \rightarrow 1, 10 \rightarrow 1,$
 177 $11 \rightarrow 0$ and the NOR gate by $00 \rightarrow 1, 01 \rightarrow 0,$
 178 $10 \rightarrow 0, 11 \rightarrow 0$, mapping two input states to one
 179 output state for the binary-based four configurations.
 180 In a similar fashion, additional logic gates can be iden-
 181 tified, e.g., AND and NOT gates.

182 Comparative classical simulations (see Supplemen-
 183 tary Information A) verified that the current is sig-
 184 nificantly (15-51%) larger in the quantum case. The
 185 increased current is due to the wave nature of the elec-
 186 trons, in particular constructive interference. For ex-
 187 ample, when both gates are driven by 0.105 V, $I_{C_2} =$
 188 $46 \mu\text{A}$ but the classical current is $28 \mu\text{A}$ ($\sim 39\%$
 189 reduction). An even stronger difference is observed for
 190 0.21 V, where $I_{C_2} = 41 \mu\text{A}$ against a classical cur-
 191 rent of $20 \mu\text{A}$ ($\sim 51\%$ reduction). A similar behav-
 192 ior is also present for repulsive symmetric potentials:
 193 For -0.105 V, $I_{C_2} = 31 \mu\text{A}$ is reduced to $21 \mu\text{A}$
 194 in the classical case ($\sim 32\%$ reduction). Furthermore,
 195 in the asymmetric case of $\phi_{G_2} = 0.105$ V and $\phi_{G_1} =$
 196 -0.105 V, $I_{C_1} = 39 \mu\text{A}$ while the classical current is
 197 $33 \mu\text{A}$ ($\sim 15\%$ reduction). These significant differences
 198 between the quantum and the classical currents clearly
 199 show, that indeed quantum effects are essential for
 200 eQILDs to allow for more distinct and thus practically
 201 usable current levels.

202 In conclusion, the introduced eQILD provides an al-
 203 ternative path towards advanced non-magnetic, low-
 204 power, and high performance classically operating logic
 205 devices. The electronic nature of eQILDs provides
 206 an attractive alternative path towards co-integration
 207 with conventional electronics. The device structure is
 208 amenable for fabrication due to simplistic geometries
 209 and established materials. Furthermore, various adap-
 210 tations are perceivable, for instance, additional gates,
 211 channels, or bias configurations would allow to intro-
 212 duce even more current states. Alternatively, the out-
 213 put channels can be arranged in a non-symmetric man-
 214 ner or can be merged outside of the device to allow for
 215 further superpositioned states. Robustness is tuneable
 216 by increasing the current ranges. The eQILD design
 217 is in principle adaptable to other transport materials
 218 (e.g. other TMDs, 2DEGs), offering additional options
 219 for practical realizations. In addition to classical bi-

220 nary logic, the manifestation of several current levels at
 221 the individual output channels provides a path towards
 222 multi-valued logic, which, although having inherent
 223 higher robustness challenges [22], promises higher in-
 224 tegration densities [23]. A particular attractive per-
 225 spective is provided considering the recent advances
 226 towards two-electron sources [5]: The eQILD opera-
 227 tion could be extended towards applications in entan-
 228 glementronics [19, 24, 25], enabling the use of entanglement
 229 for non-local classical logic.

ϕ_{G_1}	ϕ_{G_2}	I_{C_1}	I_{C_2}	I_{C_3}	GATE
-0.21	-0.21	9	10	9	NOR: 11 \rightarrow 0
-0.21	-0.105	10	14	28	
-0.21	0	13	15	36	NOR: 10 \rightarrow 0
-0.21	0.105	16	13	37	
-0.105	0.21	15	14	32	
-0.105	-0.21	28	14	10	
-0.105	-0.105	19	31	19	NAND: 00 \rightarrow 1
-0.105	0	17	11	47	
-0.105	0.105	18	13	39	NAND: 01 \rightarrow 1
-0.105	0.21	16	16	24	
0	-0.21	36	15	13	NOR: 01 \rightarrow 0
0	-0.105	47	11	17	
0	0	26	27	26	NOR: 00 \rightarrow 1
0	0.105	17	13	47	
0	0.21	14	20	34	
0.105	-0.21	37	13	16	
0.105	-0.105	39	13	18	NAND: 10 \rightarrow 1
0.105	0	47	13	17	
0.105	0.105	15	46	15	NAND: 11 \rightarrow 0
0.105	0.21	10	20	40	
0.21	-0.21	32	14	15	
0.21	-0.105	24	16	16	
0.21	0	34	20	14	
0.21	0.105	40	20	10	
0.21	0.21	15	41	15	

Table 1: Output channel quantum currents $I_{C_{1,2,3}}$ (μA) for an extended set of gate biases $\phi_{G_{1,2}}$ (V) relative to Figure 4. The GATE column shows individual rows of the truth tables of realizable NAND and NOR gates according to the rules shown in Table 2; framed current values highlight the utilized channel to realize the logic.

IN		C	OUT		GATE
0	1		0	1	
0	-0.21	2	≤ 20	> 20	NOR
-0.105	0.105	3	≤ 16	> 16	NAND

Table 2: Exemplary logic gate definitions based on ϕ_G and I_C values of Table 1: IN associates specific $\phi_{G_{1,2}}$ (V) biases with input states 0 and 1; C is the output channel number; OUT associates specific $I_{C_{1,2,3}}$ thresholds (μA) with output states 0 and 1; and GATE shows the realizable logic gate.

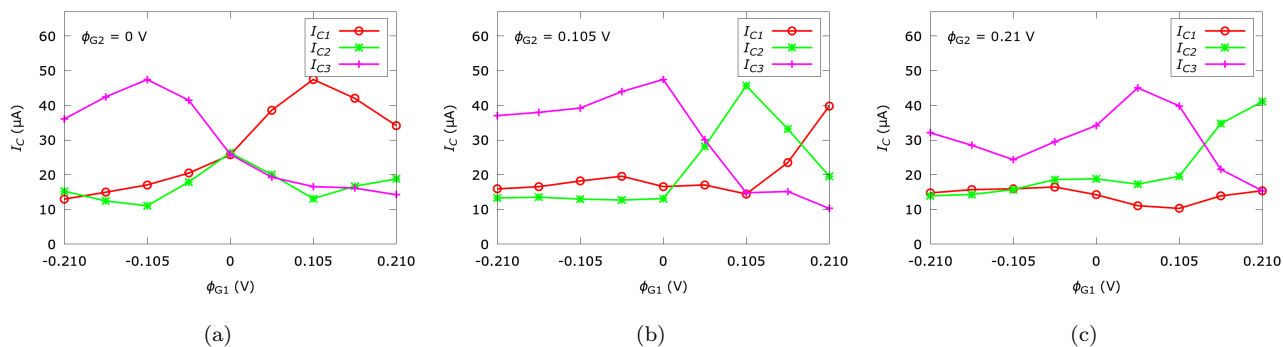


Figure 4: Output channel quantum currents $I_{C_{1,2,3}}$ for a set of gate biases $\phi_{G_{1,2}}$.

References

- [1] Bäuerle, C. *et al.* Coherent Control of Single Electrons: A Review of Current Progress. *Reports on Progress in Physics* **81**, 056503 (2018). doi:10.1088/1361-6633/aaa98a.
- [2] Yamahata, G. *et al.* Picosecond Coherent Electron Motion in a Silicon Single-Electron Source. *Nature Nanotechnology* **14**, 1019–1023 (2019). doi:10.1038/s41565-019-0563-2.
- [3] Bisognin, R. *et al.* Quantum Tomography of Electrical Currents. *Nature Communications* **10**, 3379 (2019). doi:10.1038/s41467-019-11369-5.
- [4] Fletcher, J. D. *et al.* Continuous-Variable Tomography of Solitary Electrons. *Nature Communications* **10**, 5298 (2019). doi:10.1038/s41467-019-13222-1.
- [5] Moskalets, M., Kotilahti, J., Burset, P. & Flindt, C. Composite Two-Particle Sources. *The European Physical Journal Special Topics* **229**, 647–662 (2020). doi:10.1140/epjst/e2019-900121-x.
- [6] Rodriguez, R. H. *et al.* Relaxation and Revival of Quasiparticles Injected in an Interacting Quantum Hall Liquid. *Nature Communications* **11**, 2426 (2020). doi:10.1038/s41467-020-16331-4.
- [7] Clark, L. A., Kataoka, M. & Emary, C. Mitigating Decoherence in Hot Electron Interferometry. *New Journal of Physics* **22**, 103031 (2020). doi:10.1088/1367-2630/abb9e5.
- [8] Bellentani, L., Forghieri, G., Bordone, P. & Bertoni, A. Two-Electron Selective Coupling in an Edge-State Based Conditional Phase Shifter. *Physical Review B* **102**, 035417 (2020). doi:10.1103/PhysRevB.102.035417.
- [9] Lepage, H. V., Lasek, A. A., Arvidsson-Shukur, D. R. M. & Barnes, C. H. W. Entanglement Generation via Power-of-Swap Operations Between Dynamic Electron-Spin Qubits. *Physical Review A* **101**, 022329 (2020). doi:10.1103/PhysRevA.101.022329.
- [10] Ito, R. *et al.* Coherent Beam Splitting of Flying Electrons Driven by a Surface Acoustic Wave. *Physical Review Letters* **126**, 070501 (2021). doi:10.1103/PhysRevLett.126.070501.
- [11] International Roadmap for Devices and Systems (IRDS): Beyond CMOS (2020). URL <https://irds.ieee.org/editions/2020>.
- [12] Jaklevic, R. C., Lambe, J., Silver, A. H. & Mercereau, J. E. Quantum Interference Effects in Josephson Tunneling. *Physical Review Letters* **12**, 159–160 (1964). doi:10.1103/PhysRevLett.12.159.
- [13] de Graaf, S. E. *et al.* Charge Quantum Interference Device. *Nature Physics* **14**, 590–594 (2018). doi:10.1038/s41567-018-0097-9.
- [14] Braginski, A. I. Superconductor Electronics: Status and Outlook. *Journal of Superconductivity and Novel Magnetism* **32**, 23–44 (2019). doi:10.1007/s10948-018-4884-4.
- [15] Cahay, M. & Bandyopadhyay, S. Semiconductor Quantum Devices. vol. 89 of *Advances in Electronics and Electron Physics*, 93–253 (Academic Press, 1994). doi:10.1016/S0065-2539(08)60074-8.
- [16] Illarionov, Y. Y. *et al.* Insulators for 2D Nanoelectronics: The Gap to Bridge. *Nature Communications* **11**, 3385 (2020). doi:10.1038/s41467-020-16640-8.
- [17] Ahn, C. *et al.* Growth of Monolayer and Multilayer MoS₂ Films by Selection of Growth Mode: Two Pathways via Chemisorption and Physisorption of an Inorganic Molecular Precursor. *ACS Applied Materials & Interfaces* **13**, 6805–6812 (2021). doi:10.1021/acsaami.0c19591.
- [18] Weinbub, J. & Ferry, D. Recent Advances in Wigner Function Approaches. *Applied Physics Reviews* **5**, 041104 (2018). doi:10.1063/1.5046663.
- [19] Weinbub, J., Ballicchia, M. & Nedjalkov, M. Electron Interference in a Double-Dopant Potential Structure. *Physica Status Solidi RRL* **12**, 1800111 (2018). doi:10.1002/pssr.201800111.
- [20] Ballicchia, M., Weinbub, J. & Nedjalkov, M. Electron Evolution Around a Repulsive Dopant in a Quantum Wire: Coherence Effects. *Nanoscale* **10**, 23037–23049 (2018). doi:10.1039/C8NR06933F.
- [21] Kaasbjerg, K., Thygesen, K. S. & Jacobsen, K. W. Phonon-Limited Mobility in *n*-Type Single-Layer MoS₂ from First Principles. *Physical Review B* **85**, 115317 (2012). doi:10.1103/PhysRevB.85.115317.
- [22] Mano, M. M., Kime, C. R. & Martin, T. *Logic and Computer Design Fundamentals, 5th Edition* (Pearson, 2016).
- [23] Lee, L. *et al.* ZnO Composite Nanolayer with Mobility Edge Quantization for Multi-Value Logic Transistors. *Nature Communications* **10**, 1998 (2019). doi:10.1038/s41467-019-09998-x.
- [24] Ellinghaus, P., Weinbub, J., Nedjalkov, M. & Selberherr, S. Analysis of Lense-Governed Wigner Signed Particle Quantum Dynamics. *Physica Status Solidi RRL* **11**, 1700102 (2017). doi:10.1002/pssr.201700102.
- [25] Benam, M., Ballicchia, M., Weinbub, J., Selberherr, S. & Nedjalkov, M. A Computational Approach for Investigating Coulomb Interaction using Wigner-Poisson Coupling. *Journal of Computational Electronics* (2021). doi:10.1007/s10825-020-01643-x.
- [26] Nedjalkov, M. *et al.* Wigner Equation for General Electromagnetic Fields: The Weyl-Stratonovich Transform. *Physical Review B* **99**, 014423 (2019). doi:10.1103/PhysRevB.99.014423.
- [27] Querlioz, D., Dollfus, P. & Mouis, M. *The Wigner Monte Carlo Method for Nanoelectronic Devices* (Wiley-ISTE, Hoboken-London, 2010). doi:10.1002/9781118618479.
- [28] Nedjalkov, M., Querlioz, D., Dollfus, P. & Kosina, H. *Wigner Function Approach*, 289–358 (Springer, New York, 2011). doi:10.1007/978-1-4419-8840-9_5.
- [29] Ellinghaus, P., Weinbub, J., Nedjalkov, M., Selberherr, S. & Dimov, I. Distributed-Memory Parallelization of the Wigner Monte Carlo Method Using Spatial Domain Decomposition. *Journal of Computational Electronics* **14**, 151–162 (2015). doi:10.1007/s10825-014-0635-3.
- [30] Ryu, S., Kataoka, M. & Sim, H.-S. Ultrafast Emission and Detection of a Single-Electron Gaussian Wave Packet: A Theoretical Study. *Physical Review Letters* **117**, 146802 (2016). doi:10.1103/PhysRevLett.117.146802.

Modelling Theory

The numerically solved Wigner transport equation is

$$\left[\frac{\partial}{\partial t} + \frac{\mathbf{p}}{m} \cdot \frac{\partial}{\partial \mathbf{r}} \right] f_W(\mathbf{p}, \mathbf{r}, t) = \int d\mathbf{p}' V_W(\mathbf{p} - \mathbf{p}', \mathbf{r}) f_W(\mathbf{p}', \mathbf{r}, t) \quad (1)$$

and corresponds to spatially dependent, electric fields slowly varying in time, so that magnetic effects are not involved [26]. Here, t is the time, m the electron mass, \mathbf{p} the momentum, and \mathbf{r} the spatial position; (\mathbf{p}, \mathbf{r}) spans the phase space. Furthermore, V_W is the Wigner potential operator obtained from the electric potential $\phi(\mathbf{r})$ by the Weyl transform and f_W is the Wigner function, providing physical averages by the same expressions inherent for the classical distribution function. The equation fully accounts for coherent, time-dependent quantum effects, such as tunnelling, interference, and non-locality. Despite that (1) can be augmented by terms accounting for decoherence effects of scattering [27] here we focus on the coherent behavior, governed by the complicated interplay of the physical characteristics of the electron state in terms of velocity, energy and dispersion, electric potentials and geometry.

We apply the signed-particle model to the Wigner transport equation [28]. This model extends the conventional, classical particle model applied in the Boltzmann theory by assigning quantum information to the particles. Quantum particles evolve in a classical way, however, they carry a plus or minus sign, are generated by the Wigner potential V_W , and annihilate each other if they occupy the same point in phase space. Ultimately, we solve the signed-particle Wigner transport equation by a stochastic approach, provided by our ensemble Monte Carlo solver VIENNAWD¹ [29].

The classical limit of (1) is obtained in the case of slowly varying potentials, when the Wigner potential reduces to the classical force giving rise to the ballistic Boltzmann equation [28]. Accordingly, the signed-particle model reduces to the Boltzmann model of classically evolving particles.

An electron is modelled as a minimum uncertainty wave packet, which is described by an admissible Wigner pure state [27]

$$f_W(\mathbf{r}, \mathbf{p}) = N \exp\left\{-|\mathbf{r} - \mathbf{r}_0|^2 / (2\sigma^2)\right\} \exp\left\{-|\mathbf{p} - \mathbf{p}_0|^2 2\sigma^2 / \hbar^2\right\}, \quad (2)$$

where N is a normalization constant. The state (2) is characterized by a Gaussian distribution [30] with a standard spatial deviation $\sigma = 16$ nm. This corresponds to a momentum deviation smaller than 0.1 nm^{-1} around $p_0 = 0.94 \text{ nm}^{-1}$ and also to an uncertainty of about 5 meV with respect to the kinetic energy of the injected electron.

The financial support by the Austrian Science Fund (FWF): P29406 and P33609, the Austrian Federal Ministry for Digital and Economic Affairs and the National Foundation for Research, Technology and Development is gratefully acknowledged. The computational results presented here have been achieved using the Vienna Scientific Cluster (VSC).

¹www.iue.tuwien.ac.at/software/viennawd/